Impacts of Real Hands on 5G Millimeter-Wave Cellphone Antennas: Measurements and Electromagnetic Models

Bing Xue, *Graduate Student Member, IEEE*, Pasi Koivumäki, *Member, IEEE*,
Lauri Vähä-Savo, *Graduate Student Member, IEEE*, Katsuyuki Haneda, *Member, IEEE*,
and Clemens Icheln

Abstract— Penetration of cellphones into markets requires their robust operation in time-varying radio environments, especially for millimeter-wave communications. Hands and fingers of a human cause significant changes in the physical environments of cellphones, which influence the communication qualities to a large extent. In this article, referential cellphone antenna arrays at 28 and 39 GHz are designed, and then simplified electromagnetic (EM) models of them for simulations are developed. Their radiation properties are evaluated through near-field scanning of the two prototypes in free space, first for de-embedding the feedline loss of cellphone antennas. The similarity of radiation patterns between simplified models and cellphone mock-ups ensures the reliability for comparing the simulated and measured results involving real hand effects. Next, hand–antenna interaction radiation measurements are set up so that we validate radiation performance simulations that use computational models of real hands that are generated by the approach in Vaha-Savo et al. (2022) and cellphones, by carrying out measurements of the same real hands and cellphone mock-ups and comparing measured with simulated results, which we show to agree well. This enables future research and development of mm-wave handset antennas relying on realistic simulations during the design phase.

Index Terms— Cellphone antenna array, electromagnetic (EM) antenna–human interaction, hand modeling, millimeter-wave, real hands, spherical coverage.

I. INTRODUCTION

DEMANDS of mobile users for high-data-rate communications and access to information through wireless channels have always been increasing. Sub-6-GHz radio frequencies (RFs) cannot serve all possible scenarios of radio communications, especially the high-data-rate communications for a high density of mobile users. Therefore, millimeter-wave communications attract the attention of the research community in recent years. Among the two operated bands of the frequency range of 5G cellular, the frequency

range 2 (FR2) spanning between 24.5 and 43 GHz imposes more stringent challenges to ensuring robust operations in dynamic environments than frequency range 1 (FR1) which covers lower frequency band [2]. One of the challenges is the sensitivity of antennas to the radio environment [3], [4], [5], [6]. When antennas and arrays are covered by dielectric objects such as bodies, fingers, and hand palms of the device operator, significant changes in their radiation properties are inevitable because of blockage and absorption of radiated fields. It is thus a goal of antenna designers of communication devices to minimize the detrimental effects of close-by objects on antennas [6]. There are articles studying the antenna–human interaction at above-6 GHz RF, including FR2 [1], [7], [8], [9], [10], [11], [12], [13], [14], [15], [16], [17], [18], [19], [20], [21], [22], [23], [24], [25], [26], [27]. These articles included works reporting numerical models of humans to run full-wave simulations of antenna–human interaction, e.g., [16], [17], [18], and those measuring link blockage by human bodies, e.g., [9], [10], [11]. They mainly cover human blockage effects at far fields of antennas, while articles [21], [22], [23], [24], [25], [26] discussed near-field effects of a human body on cellphone antenna radiations such as fingers', hand palms', or the whole hands' effects. For a repeatable study of hand effects, [1] and [27] established real hand models by photogrammetry and laser scanning that can be used in full-wave simulations of antenna–hand interaction. The overarching problem of the existing works reporting antenna–hand interaction is, however, *lack of comparisons between the simulations and measurements* to cross-validate the simulation models and measurement methods. [1] reported the approach for creating 3-D models of real hands and proved the importance of creating hand models for different persons. This article aims to implement measurements to compare the measured and simulated antenna–hand interaction based on the 3-D models generated by the approach in [1] and real hands in millimeter-wave bands. Although [12], [13], [14], [22], [23], [24], [25], [26] reported antenna measurements with real human effects at millimeter-wave frequencies, they hardly discussed verification of the measurement results with the corresponding simulation results. We thereby consider the verification with real human effects as the main challenge, specifically because:

1) the postures and antenna positions of the simulation model and the experiments with the real human should be the same as much as possible. Differing from low frequencies, the realized radiation characteristics of antennas are more sensitive to a small change in human postures [28];

2) the human posture under measurement should stay as stable as possible over time, especially at millimeter-wave frequencies [6], [29]. As opposed to hand phantoms, tiny movements of a human body are inevitable even during a relatively short measurement duration of, e.g., 1 min.

These measurement challenges are solved in the article based on the near-field scanner. The innovations reported in this article are as follows:

1) the introduction of referential antenna arrays for antenna–obstacle interaction studies. They are the simplest manufacturable antenna array on cellphone-sized chassis at 28 and 39 GHz, realized by dual-polarized patches;

2) setups of antenna–hand interaction measurements showing an acceptable degree of repeatability for a limited amount of measurement time, despite involving nonrepeatable real human hands; and finally,

3) cross-verified electromagnetic (EM) simulation models and measurement methods of the antenna–human interaction analysis at 28 and 39 GHz; the simulation models include 3-D hand models of real humans, and the measurements are done with the corresponding real human hands.

The rest of this article is arranged as follows. Section II introduces our designs of referential dual-polarized antenna arrays for 28 and 39 GHz, including antenna elements, feed lines, and cable connectors enclosed in a cellphone chassis. Section III summarizes human hand models and their integration with the antenna array models. Section IV first introduces impedance matching and isolation characteristics of the manufactured antenna array. Then the principle of radiation measurements for antenna arrays is elaborated where an approach to de-embedding the losses of measurement setups is introduced. Section V details measurement setups with real hands, paying attention to the fact that each measurement must be completed while a subject human hand stays still. The measurements give evidence for the cross-validation of the simulation models and measurement approaches at the two frequencies. Finally, conclusions are summarized in Section VI.

II. REFERENTIAL MILLIMETER-WAVE CELLPHONE ANTENNA ARRAY

Referential antenna arrays are essential to analyze antenna–obstacle interaction. An array of electric and magnetic Hertzian dipoles would have been an ideal referential antenna, but it is not possible to manufacture them. Our referential arrays are therefore defined as the simplest manufacturable

---

[1]In this article, the spherical-coordinate variable θ starts from the positive direction of the z-axis; another spherical-coordinate variable ϕ starts from the positive direction of the x-axis.
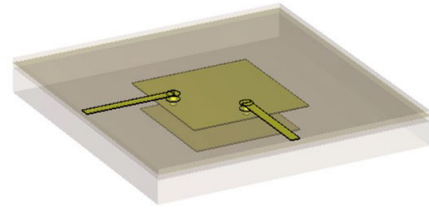

Fig. 1. Dual-polarization microstrip-feed antenna structures, bottom view, with transparent ground plane and substrates.

array based on patches, which are capable of low-profile and dual-polarized implementation and show broad beams and hence can be installed at various locations of the cellphone [4], [15], [16], [23], [25], [30], [31]. To emulate the cellphone chassis and connect the antennas to measurement devices, the cellphone chassis and feeding structures also need to be fabricated and designed. The designs and fabrications of two referential dual-polarized patch antenna arrays on a cellphone chassis are introduced. They are used for the experimental antenna–hand interaction studies at 28 and 39 GHz.

A. Antenna Element Design

Millimeter-wave cellphone antennas are usually designed using patches [16], [21] due to their directivities illuminating the half-hemisphere and possibilities of dual-polarized arrays with suitable isolation between antenna ports. Two patch antennas are designed to cover 28- and 39-GHz bands, as representatives of FR2; a single patch antenna cannot cover the two bands because patch antennas usually cover only up to 10% relative bandwidth. Stacked patches and via-feeding are used for wideband impedance matching at the two bands as shown in Fig. 1, which depicts the schematic of the antenna, seen from its bottom side implementing a ground plane. For 28 GHz (39 GHz), the dimension of the patch is 2.55×2.55 mm^2 (1.76×1.76 mm^2), and the dimension of the parasitic patch is 2.30×2.30 mm^2 (1.53×1.53 mm^2). The dimension of the patch antenna along with the diameter of void rings for vias was optimized for the desired impedance bandwidth. It is worth noting that the impedance bandwidth of each antenna element should be large enough to ensure the robustness of antennas' radiation performance against possible manufacturing errors and detuning effects attributed to dielectric loading of human tissue during antenna–human interaction measurements. We set over 1-GHz bandwidth as enough in this study.

B. Antenna Array Design and Fabrication

The dual-polarized stacked patches are used to form 4-element linear antenna arrays on a 150×69 mm^2 printed circuit board (PCB) for 28 GHz and on a 150×75 mm^2 PCB for 39 GHz as illustrated in Figs. 2 and 3, respectively. Each element has two ports, of which the main polarization is orthogonal to each other. The PCB consists of three layers of substrates, i.e., 0.5-mm-thick top substrate (MEGRTON6 5775G: $\epsilon_r = 3.62$, loss tangent: 0.005 at 28 GHz and
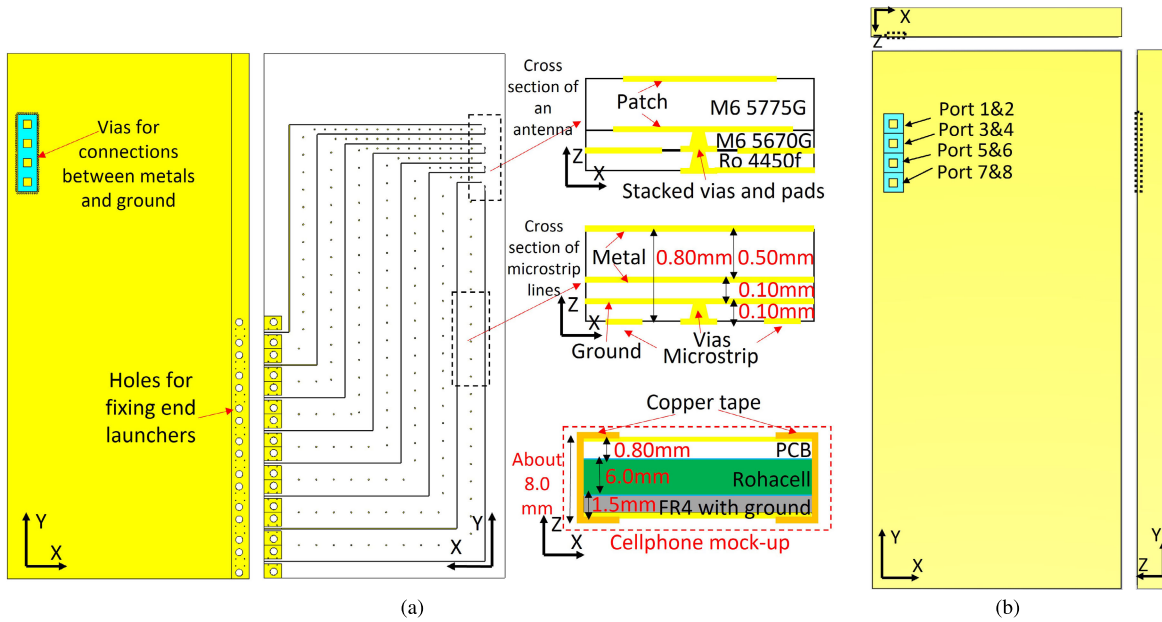
Fig. 2. (a) Top and bottom views of the antennas and feeding lines at 28 GHz. Cross sections of an antenna and microstrip line. Cyan and white parts represent the substrates while yellow parts are metal. A cellphone mock-up, consisting of the PCB, a Rohacell, and FR4 substrate, is shown in the stackup indicated by the red dashed rectangle. (b) Schematic of simple antenna array configurations from the top views and the side views of a metal phone chassis at 28 GHz ($69 \times 150 \times 8$ mm^3).
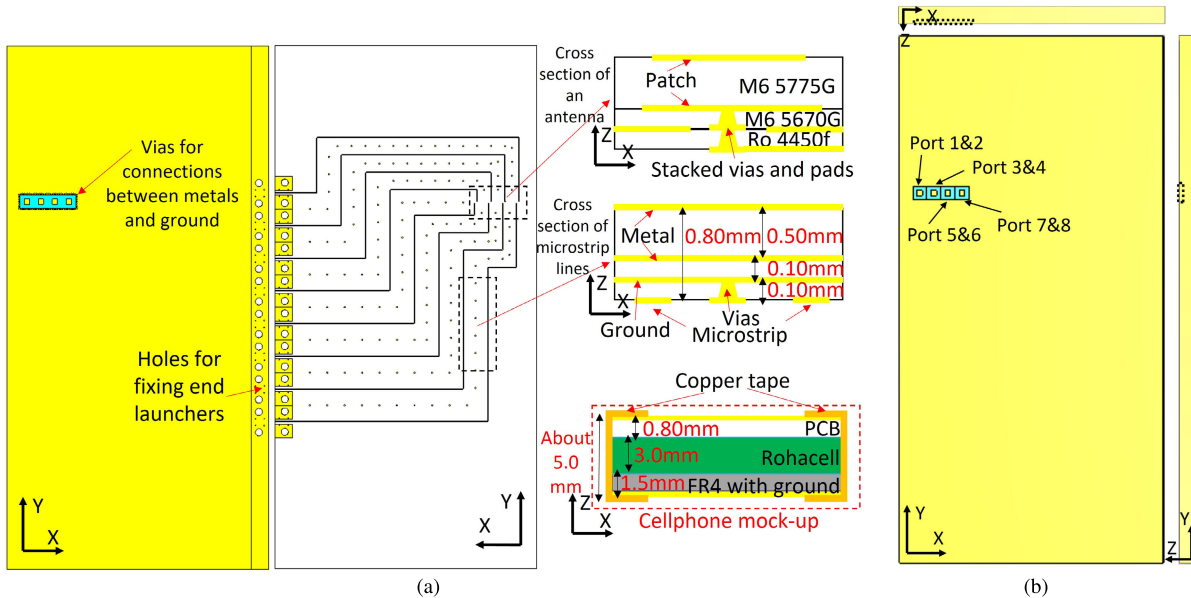

Fig. 3. (a) Top and bottom views of the antennas and feeding lines at 39 GHz. Cross sections of an antenna and microstrip line. Cyan and white parts represent the substrates while yellow parts are metal. A cellphone mock-up, consisting of the PCB, a Rohacell, and FR4 substrate, is shown in the stackup indicated by the red dashed rectangle. (b) Schematic of simple antenna array configurations from the top views and the side views of a metal phone chassis at 39 GHz ($75 \times 150 \times 5$ mm^3).

0.006 at 39 GHz), 0.1-mm-thick middle substrate (MEGR-TON6 5670G: $\epsilon_r = 3.22$, loss tangent: 0.005 at 28 GHz and 0.006 at 39 GHz), and 0.1-mm-thick bottom one (Rogers 4450f: $\epsilon_r = 3.70$, loss tangent: 0.004). The thickness of copper is 35 μm for the top and bottom substrates while it is 18 μm for the middle due to the manufacturer's ability. The vias surrounding the antenna array connect the metal layers of the top and middle substrates to reduce surface waves on the PCB. Long feeding lines have to be used to connect the antennas to

eight end-launch connectors (*Southwest Microwaves* 2.40-mm narrow type) to minimize radiation from the connectors. The feed line width is 0.20 mm, while via pads and laser-drilled microvias are 0.40 and 0.15 mm in diameter, respectively, as shown in the cross-sectional schematic of Figs. 2 and 3. A void ring of 0.30-mm diameter is used to avoid the connections between ground and feed vias. Apart from the mentioned vias, the parallel vias to the feed lines reduce coupling between the feed lines while those near connectors

ensure the galvanic connection between the top and bottom substrates. As the PCB is only 0.8-mm thick, to enhance its mechanic strength and emulate the practical cellphones, 6- and 3-mm-thick Rohacell foam was attached to the 28- and 39-GHz PCBs, along with 1.5-mm-thick FR4 with grounds. The Rohacell foam, which has a low permittivity close to the air and a low loss tangent of 0.002, minimizes losses of the RF signals in the feed lines. In addition, the copper tapes were used to further enhance the electrical connections between the grounds of FR4 and millimeter-wave PCBs. Inside red dotted rectangles of Figs. 2 and 3 show a cross-sectional view of the whole phone mock-ups. The two mock-ups are different in their widths, antenna array directions and locations, and connector locations. Finally, to include the roughness effect of the copper on high-frequency PCBs, 0.4 μm roughness of the copper surface [32] was applied to the cellphone mock-up simulations.

III. SIMULATION MODELS OF ANTENNA–HAND INTERACTION

The EM simulation models of the antenna–hand interaction are presented in this section. Following a brief introduction to the hand modeling approach, simplified antenna models are provided for feasible antenna–hand simulations.

A. Photogrammetry Modeling a Human Hand

The radiation patterns of the cellphone antenna arrays are influenced by the posture of the hand holding the phone. Developing many hand models for antenna–hand interaction simulations is viable. An approach to obtaining 3-D human hand models was reported in our prior article [1]. The approach consists of the following four steps: 1) taking a video of a hand holding a transparent cellphone-sized box; 2) extracting many pictures from the video and using *Autodesk Recap Photo* to generate a 3-D initial hand model; 3) completing the hand model by, e.g., filling a hole, using the software *CloudCompare* and *Autodesk ReCap Photo*, and finally, 4) importing them into EM solvers, e.g., *CST Studio Suite*.

B. Simplified Antenna Models

Simplified models of cellphone antenna arrays at 28 and 39 GHz are illustrated in Figs. 2(b) and 3(b), respectively. The simplified arrays consist of patch antennas integrated on a copper cellphone chassis using the same substrates as the complete antenna array models in Figs. 2(a) and 3(a). The chassis size is the same for the complete and simplified arrays as well as the copper surface roughness of the antenna arrays. However, the simplified arrays are fed by discrete ports and do not include feed lines or cable connectors. Solving EM simulations with the simplified models is much quicker than those with the complete models. Furthermore, the simplified models are used as a reference to de-embed the losses of the feed lines and cable connectors of the complete array models during measurements. The de-embedding allows us to focus on antenna radiation performance, which is difficult to measure without feed lines or connectors. Cross-verification of the simplified models and the manufactured prototypes is performed in Section IV by comparing radiation patterns.
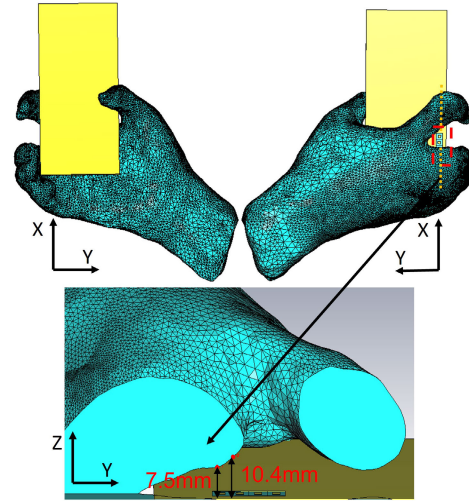

Fig. 4. Top and bottom views of the hand with 28-GHz phone mock-up; the cross section along the antenna array with the normal distance between antennas and the hand model.
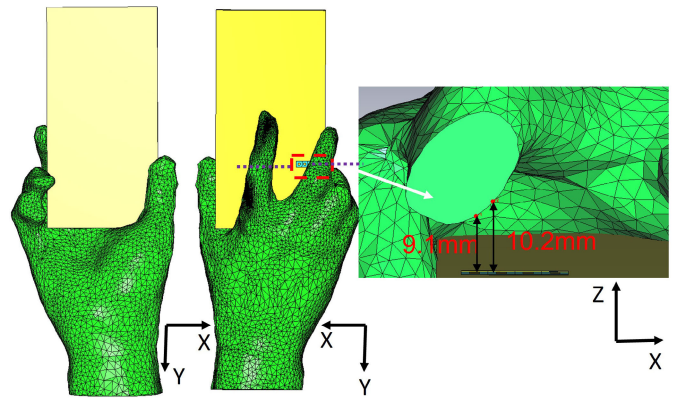

Fig. 5. Top and bottom views of the hand with 39-GHz phone mock-up; the cross section along the antenna array with the normal distance between antennas and the hand model.

C. Antenna–Hand Models

Figs. 4 and 5 show the hand models generated by the approach in [1] and integrated with the simplified cellphone chassis. They are the *exact* postures of hands during antenna array measurements detailed in Section V. Some dimensions are also shown in the figure as they are important for the patch antennas not to suffer from impedance matching degradation due to proximity hand tissue. The permittivity of the hands is chosen to be that of dry human skin, i.e., $\epsilon_r = 16.55$ and $\sigma = 25.82$ S/m at 28 GHz; $\epsilon_r = 11.98$ and $\sigma = 31.43$ S/m at 39 GHz [1], [33].

IV. ANTENNA ARRAY MEASUREMENTS IN FREE SPACE

The principle and setups for free-space antenna array measurements are described in this section. Impedance bandwidth, isolation, and radiation characteristics of the manufactured referential arrays are compared with those from simulations.

A. Input Reflection Coefficients and Mutual Coupling

The reflection coefficients of the scattering parameter were measured for each port of 28 and 39-GHz phone mock-up
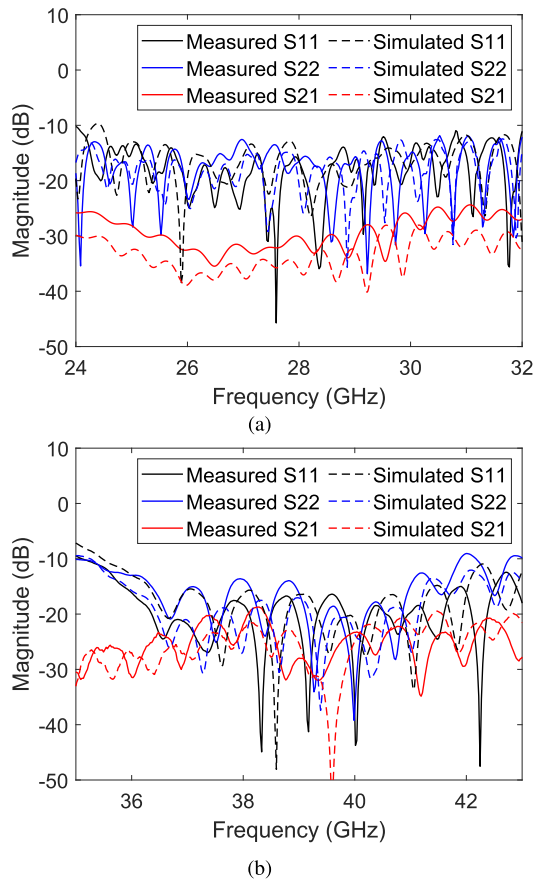
(a)

(b)

Fig. 6. Reflection coefficients and mutual coupling of two exemplary ports 1 and 2 for (a) 28-GHz and (b) 39-GHz cellphone mock-ups.
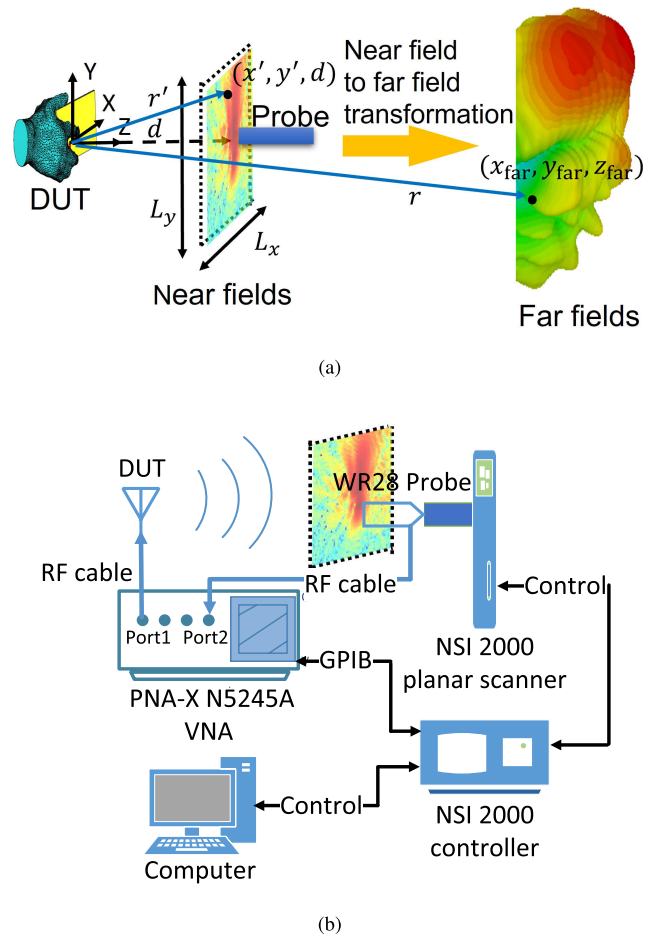

(a)

(b)

Fig. 7. (a) Definitions of our near-field measurements and far-field observation points and (b) schematic of the near-field measurement system for far-field radiation patterns.

using the PNA-X N5245A vector network analyzer (VNA). The calibration function of the VNA was applied from 20 to 50 GHz. The bandwidth of intermediate frequency was 1 kHz. Two representative ports were selected to show impedance matching and mutual coupling in Fig. 6. The ports' names are defined in Figs. 2(b) and 3(b). The simulations and measurements show a close agreement although there is an about 400-MHz band shift for the 39-GHz phone mock-up in Fig. 6(b). Still, antennas have wide-enough impedance bandwidth to radiate.

B. Principle of Radiation Measurements

The schematic of the radiation pattern measurement by planar near-field scanning is shown in Fig. 7(a). Spacing between two adjacent near-field sampling points along the x- and y-axes is Δx and Δy, respectively; d is the normal distance between the antenna array under the test and the probe scanning plane. The measured tangential electric field components of the near fields on the probe scanning plane are transformed into far fields. The relevant formulas and working mechanisms are described in Appendix.

In the near-field to far-field transformation, the measurement error due to probe's radiation patterns needs to be calibrated. The calibration compensates for the phase and amplitude of the far-field radiation pattern over the front hemisphere around the probe [34]. In this work, the standard rectangular open-ended

waveguide is used as the probe. The approximate formulas for the radiation pattern of an open-ended waveguide [35] are used for probe compensation.

C. Free-Space Measurements

Free-space measurements are performed to verify the near-field to far-field transformation method and to estimate losses of the measurement system for de-embedding, serving for calibration.

The schematic of the near-field scanner system is shown in Fig. 7. A standard rectangular WR28 waveguide was used as the field probe installed on the NSI2000 planar scanner. The PNA-X N5245A network analyzer was used to measure the transmission coefficients of the scattering parameter between the antenna under test and the field probe. A computer-controlled positioning of the planar scanner for the waveguide probe was done along with acquisition of the transmission coefficients. The bandwidth of intermediate frequency in the VNA was 10 kHz, while its output power was 5 dBm. When measuring the two polarizations E_x and E_y of E in (2), it was necessary to repeat the scanning for each polarization after changing the waveguide orientation by 90°.

TABLE I
SETUPS OF NEAR-FIELD SCANNING FOR CELLPHONE MOCK-UPS
IN FREE SPACE AND WITH HAND EFFECTS

	Free Space		With Hand	
Frequency [GHz]	28	39	28	39
d [mm]	20	20	50	50
Δx [mm]	5	4	5	4
Δy [mm]	5	4	5	4
L_x [mm]	400	300	200	200
L_y [mm]	400	300	200	200
Measurement time for a single port [min.]	100	80	12	15
Only major polarization	No	No	Yes	Yes

TABLE II
ESTIMATED LOSSES OF EACH PORT OF THE ARRAYS DUE TO
THE MICROSTRIP LINE OF THE MANUFACTURED ARRAY

Ports	28 GHz	39 GHz
1	9.4 dB	9.8 dB
2	8.9 dB	10.7 dB
3	9.6 dB	9.9 dB
4	9.8 dB	10.1 dB
5	9.3 dB	9.7 dB
6	10.1 dB	9.6 dB
7	9.8 dB	9.2 dB
8	11.3 dB	9.0 dB

In practice, the fast and accurate near-field measurements should meet some requirements.

1) the normal-direction spacing d between antenna elements and the probe should be 1–5 wavelengths of the frequency of interest;
2) the measurement steps Δx, Δy along the x- and y-axes should be smaller than 0.5 wavelengths;
3) the limited scanning area S_0 is chosen as long as the power density of the radiated field from the antenna under test is small enough outside the area and the signal–noise ratio (SNR) of the received signal at the VNA is high. However, the low power density outside the area S_0 and high SNR cannot be always achieved simultaneously. Accordingly, a tradeoff between the power density and SNR is considered.

The setups of 28- and 39-GHz near-field scanning are defined based on the specific measurement setup as shown in Table I. In the measurements, the size of S_0 is based on: 1) the power density on the boundary of S_0 is smaller than 30 dB compared with the maximum power density inside the area S_0 and 2) the SNR is larger than 20 dB inside the area.

D. De-Embedding the Losses of the Measurement System and Microstrip Lines

During the near-field to far-field transformation, the far-field locations are at infinite distances from the antenna array, i.e., $r = \infty$. A standard gain horn was introduced as a probe to estimate the whole measurement system losses, including the radio frequency cables, the near- to far-field transformation method, and cable connectors. As shown in Figs. 2 and 3, the manufactured antenna arrays are with different lengths of the feed lines. In addition to the system loss estimates, the losses of feed lines of the antenna array are important quantities to be de-embedded from the measured radiation patterns of the antenna arrays. Their losses are estimated by the average difference between the simulated and measured main beams in free space [16]. Numerically simulated far fields of the simplified antenna models in Figs. 2(b) and 3(b) are used as the reference in estimating the losses, while the measurements cover $\phi \in [0°, 360°]$ and $\theta \in [0°, 60°]$ since the far fields are only valid for $\theta \leq 60°$ in the near-field scanner; refer to Fig. 7(a) for the coordinate system; θ and ϕ denote the polar and azimuth angles, respectively. The loss estimates of each

port for the two prototypes are shown in Table II, indicating that they are proportional to the lengths of the feed lines.

After de-embedding the losses, the elevation cuts of the realized gains in free space are shown in Fig. 8 for the selected ports of the two cellphone mock-ups. "H" or "V" shows the vertical or horizontal polarization, respectively, of ports based on the coordinates in Figs. 2(b) and 3(b). The simplified models' radiation patterns are similar to those of the manufactured prototypes with a maximum difference of 1.5 dB, indicating that the simplified models are good representative models of the manufactured prototypes.

The loss estimates in Table II are also applied to the far-field patterns derived from the near-field measurements, both with and without hand effects. The phase shift of the microstrip line is not shown since we only focus on statistical characteristics of beam-formed arrays. In the latter, evaluation metrics will be introduced, and the detuning effects of real hands on the antenna arrays are avoided as will be elaborated in Section V.

E. Array Beam Synthesis and Spherical Coverage

Spherical coverage is an empirical statistic of the maximum gains that an antenna array can realize for all feasible angles on a sphere, hence has been one of the important figure-of-merits of millimeter-wave antenna arrays [16], [36], [37]. When synthesizing a pattern of the array from those of individual antenna ports, equal gain combining is used for each polarization to define complex weights assuming that a single plane wave is incident. For a specific angle $\mathbf{\Omega} = (\theta, \phi)$, the realized gain of the array after the equal gain combining is given by $\hat{G}(\mathbf{\Omega}) = (|E_\theta(\mathbf{\Omega})|^2 + |E_\phi(\mathbf{\Omega})|^2)^{1/2}$ where $E_\theta(\mathbf{\Omega})$ and $E_\phi(\mathbf{\Omega})$ are the complex electric fields after the array synthesis for θ- and ϕ-polarized electric fields. Then its cumulative plot can be defined by

$$\text{CCDF}(g) = \text{prob}(\hat{G}(\mathbf{\Omega}) >= g) \tag{1}$$

where $\text{prob}(\cdot)$ is a probability operator yielding values between 0 and 1. When implementing the spherical coverage statistics, any chosen angles $\mathbf{\Omega}$ must be uniform on the whole sphere, which means the number of azimuth angle samples is smaller at smaller polar angles. The uniform grid over the whole sphere can ensure that adjacent points are with the same angular distance [38]. In this article, 4000 points are chosen to be uniform over the valid angle range, i.e., $\phi \in [0°, 360°]$ and $\theta \in [0°, 60°]$. The spherical coverage statistics are valid even
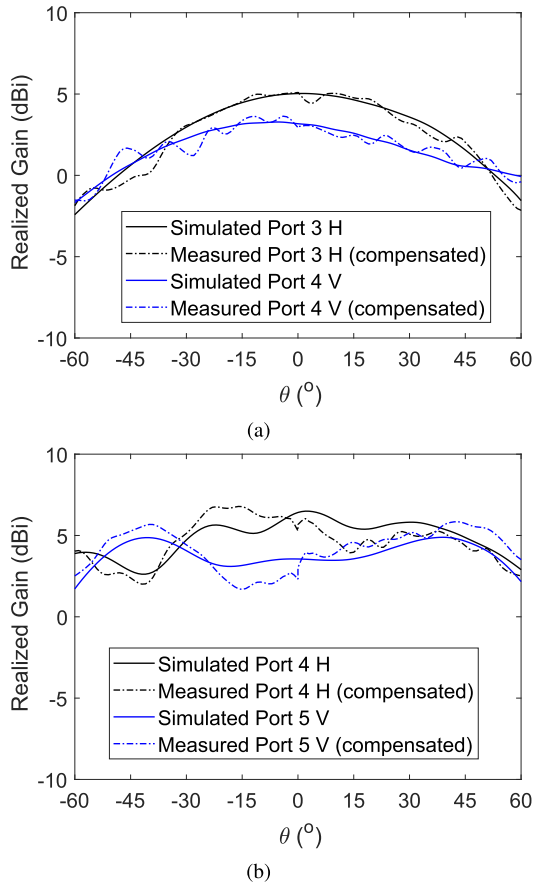
(a)

(b)

Fig. 8. Elevation cuts of the realized far-field gains in free space for (a) 28-GHz mock-up (Port 3 H and Port 4 V) and (b) 39-GHz mock-up (Port 4 H and Port 5 V) obtained by planner near-field scanning. The spherical coordinate systems are defined on the Cartesian coordinate system in Figs. 2 and 3.
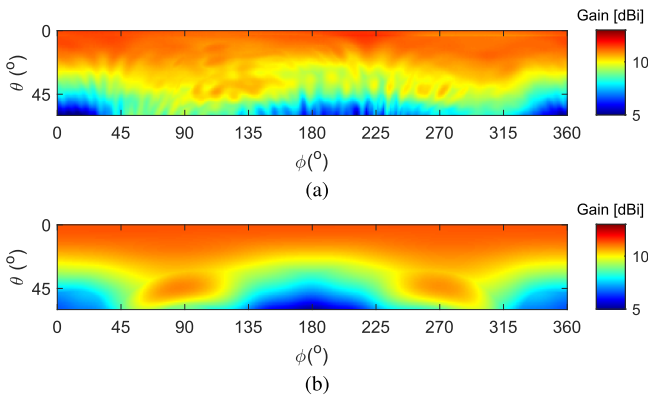

(a)

(b)

Fig. 9. Spherical coverage of the realized gains in free space for the 28-GHz mock-up. (a) Measurement and (b) simulation. The spherical coordinate system is defined on the Cartesian coordinate system in Fig. 2.

if the antenna array cannot steer beams to the whole angular range.

The spherical coverage of the 28- and 39-GHz cellphone mock-ups is shown in Figs. 9 and 10, respectively. The gain distributions are quite similar although some ripples can be seen in the measurement results. The complementary cumulative distribution function (CCDF) of the spherical coverage is computed using (1). In Fig. 11, the gain differences for
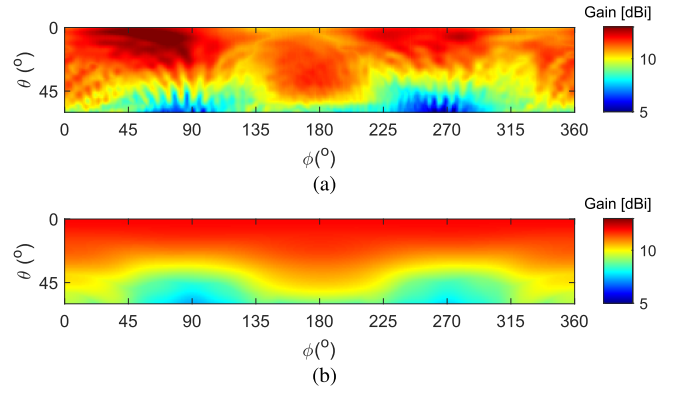

(a)

(b)

Fig. 10. Spherical coverage of the realized gains in free space for the 39-GHz mock-up. (a) Measurement and (b) simulation. The spherical coordinate system is defined on the Cartesian coordinate system in Fig. 3.
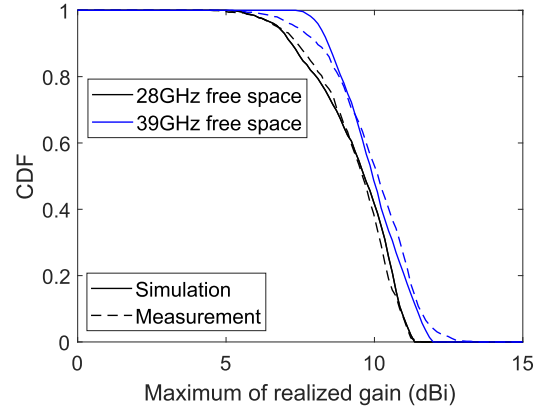

Fig. 11. CCDF of spherical coverage for the free-space case.

the 28-GHz cellphone mock-up are smaller than 0.5 dB. For the 39-GHz cellphone mock-up, the gain differences are observed at CCDF > 0.15 and CCDF < 0.95, while the difference is below 0.5 dB at the median level. The mentioned comparisons between the simulations and measurements show the validity of the simplified antenna array model and the array measurement method through near- to far-field transformation and loss de-embedding.

V. MEASUREMENTS OF ANTENNA–HAND INTERACTION

Having established the radiation pattern measurement method in free space, in this section, our approaches of real hand measurements and their results are shown.

A. Measurement Setups for Arrays Held by a User

The measurement setups for radiation patterns with hand effects differ from those for the free-space case. This is because some parts of a hand are close to antenna elements in the cellphone mock-up, thereby needing some space between them to avoid the detuning effects. Therefore, the distance d should be larger than the free-space measurements. Moreover, hand-tremble effects during the measurements are inevitable for real human bodies that could influence the accuracy of the radiation pattern measurements. The measurement time for each antenna port should be as short as possible to reduce the
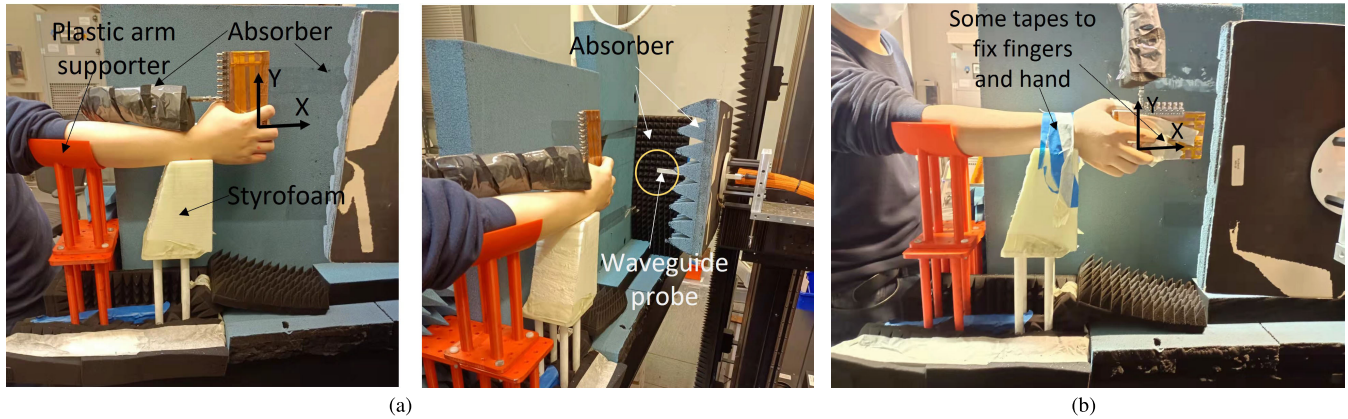
Fig. 12. (a) Two different views of the measurement setups for the 28-GHz antenna array with a human operator. (b) View of the measurement setups for the 39-GHz antenna array with a human operator.

hand-tremble effects while maintaining the accuracy. To this end, the cellphones are fixed either vertically or horizontally next to the near-field scanner so that only the major polarization of each antenna is measured using the probe. While both E_x and E_y components are measured at the probe in the free-space case, in the antenna–hand interaction measurements, only one of them corresponding to the major polarization is measured. The other polarization component is expected to be much weaker than the major polarization due to the vertical or horizontal fixing of the cellphone mockup. In the measurements, the size of S_0 is based on 1) the power density on the boundary of S_0 is smaller than 20 dB compared with the maximum power density inside the area S_0 and 2) the SNR is larger than 20 dB inside the area. Parameter settings of the near-field scanning are presented in Table I.

This elaborated setup allows us to measure each port within 12 and 15 min for 28 and 39 GHz, respectively. The following additional measures are taken to keep the hand posture stable and minimize the impact of varying permittivity of human skin from one part of a hand to another and from one human subject to another:

1) plastic supporters are designed to fix arms: they are made by a 3-D printer using the material with the dielectric constant <5 and are put far enough from the antenna array, so that it affects radiations of antennas minimally;

2) styrofoam supporters are designed to fix wrists: due to their dielectric constant $\epsilon_r \approx 1$, it can be used near the antenna arrays and hardly influences the radiation patterns of antennas;

3) absorbers are used to reduce unwanted reflections from the metal cable;

4) if necessary, thin article tapes are used to fix fingers close to antenna elements and movable parts of hands, like wrists;

5) hands are washed using soaps and then dried before the measurements to clean grease on the skin; and finally,

6) some pivotal dimensions and locations of the hands and cellphone mockups are marked on them and/or recorded by taking photos; as each port measurement requires more than 10 min, the human holding the mock-up must

have a break before the total eight ports are covered. The pivotal locations are needed for recovering the postures after each break.

The realized measurement setup is shown in Fig. 12(a) and (b). After the antenna–hand measurements, the 3-D models of the hands were obtained. The same postures were recovered by the elaborated setup mentioned above, but a transparent box having the same volume as the cellphone mockups was held to follow the approach in Section III-A. The generated 3-D hand models with a phone chassis are shown in Figs. 4 and 5.

B. Results and Discussions

Before comparing the measured and simulated radiation patterns, implications of measuring only the major polarization of the radiated near electric fields, i.e., either E_x or E_y, on the realized accuracy of the pattern estimates are discussed. To this end, a near electric field distribution E is generated by simulations where the steps Δx and Δy, the size of the area S_0, and the distance d are set according to those of hand measurements in Table I. Using the near- to far-field transformation introduced in Section IV-B and applying the loss de-embedding elaborated in Section IV-D, the spherical coverage of the 28-GHz cellphone mock-up yielded a plot in Fig. 13. A plot derived from the simulated far fields by the CST Studio is also included in Fig. 13(d), which bypasses our transformation from near- to far-fields. While Fig. 13(c) shows more ripples than Fig. 13(d) because of considering only the major polarization, the gain distributions are quite similar. The plots from the two repeated measurements in Figs. 13(a) and (b) also indicate ripples as in Fig. 13(c). However, the gain distributions of measurements are still like the two plots from simulations. By comparing the plots from two different measurements of the same posture and chassis location in Fig. 13(a) and (b), it can be seen that Fig. 13(a) shows relatively large ripples of around 7.5 dB when $\phi \in [110° \ 180°]$ while Fig. 13(b) has smaller ones of around 1.5 dB. Moreover, the high-gain angular range of the spherical coverage in Fig. 13(b) is larger than that in Fig. 13(a). This is because of random hand tremble effects
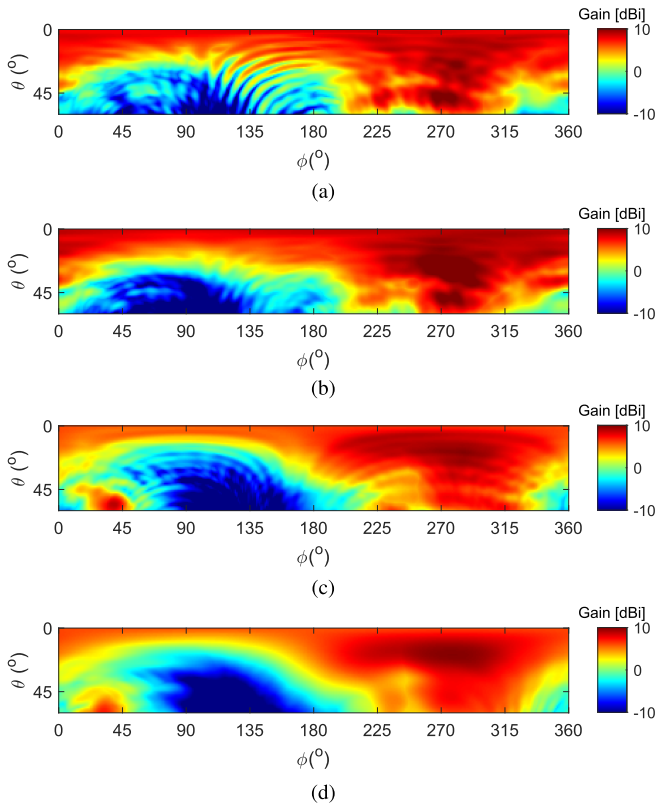
Fig. 13. Spherical coverage of the realized gains of the 28-GHz phone mock-up when held by an operator. (a) First measurement, (b) second measurement (the radio frequency cables between all the devices were disconnected and then reassembled after the first measurement), (c) near-field simulation with transformation, and (d) far-field simulation. The spherical coordinate system is defined on the Cartesian coordinate system in Fig. 12(a).

Fig. 15. Spherical coverage of the realized gains of the 39-GHz phone mock-up when held by an operator. (a) First measurement, (b) second measurement (the radio frequency cables between all the devices were disconnected and then reassembled after the first measurement), (c) near-field simulation with transformation, and (d) far-field simulation. The spherical coordinate system is defined on the Cartesian coordinate system in Fig. 12.
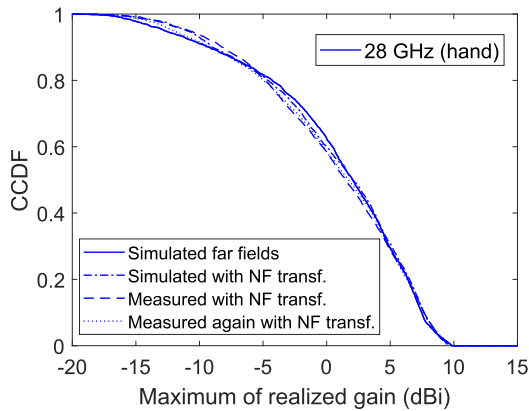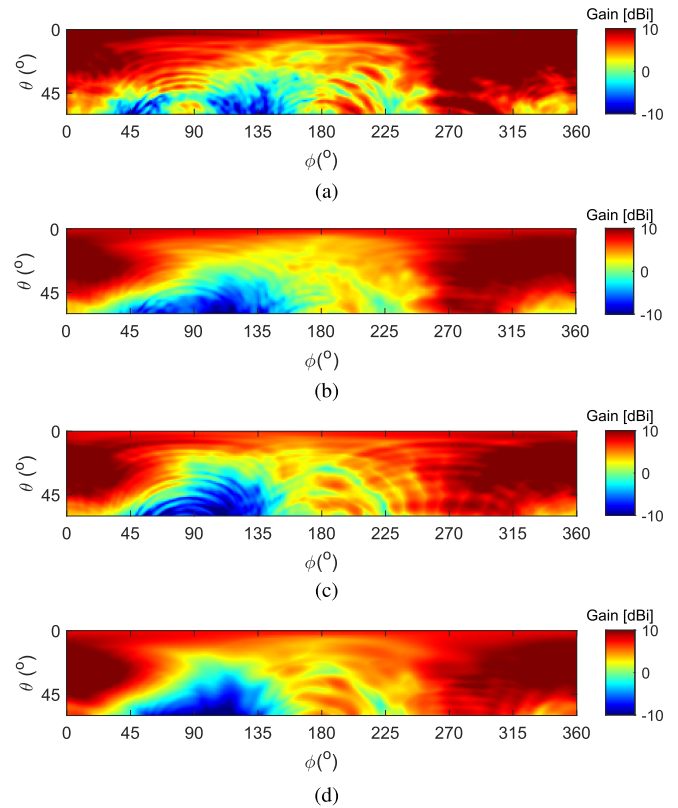

Fig. 14. CCDF of the spherical coverage for the 28-GHz phone mock-up held by a hand. "NF transf." represents near-field to far-field transformation.
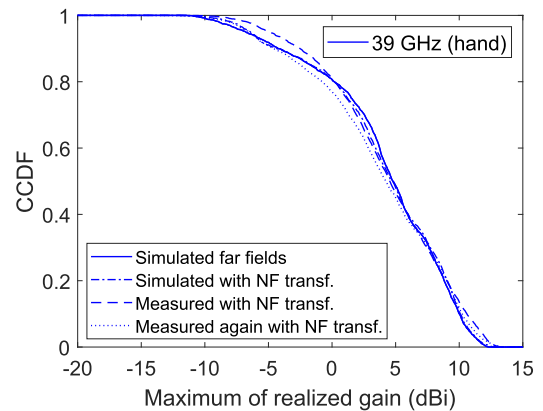
Fig. 16. CCDF of spherical coverage for the 39-GHz phone mock-up held by a hand. "NF transf." represents near-field to far-field transformation.

and slight but inevitable difference of the hand posture for the repeated measurements. Comparisons of their CCDF plots are shown in Fig. 14. There is up to 0.3-dB difference between the two simulation results, indicating that consideration of only the major polarization does not deteriorate the accuracy of estimating the spherical coverage CCDF. Differences between the two repeated measurements and the two simulations are less than 0.6 and 1.0 dB at the median and 0.9 levels of the CCDF. The two measurements show differences of smaller than 0.5 dB in the CCDF, showing repeatability

of the measurement setup despite involving nonrepeatable human hands. Moreover, although measurement uncertainty due to nonrepeatable hand effects brings about large ripples at $\phi \in [110° \ 180°]$ on the spherical coverage, they do not influence the CCDF curves noticeably.

The spherical coverage of the 39-GHz cellphone mock-up is calculated in Fig. 15. Like 28 GHz, there are more ripples on the spherical coverage simulated from the near-field data than that from the far-field data. The plot from the measurement shows similar gain distributions as simulations, although there

are more ripples like the plot derived from the near-field simulation. More ripples are in general observed both on 28- and 39-GHz plots when derived from the near-field distributions with only major polarization considered. CCDF plots of spherical coverage in Fig. 16 show a negligible difference between the two simulations, but more differences between the simulations and measurements. At 0.9 and 0.1 levels, the differences are about 1 dB for the first measurement, while, at the 0.5 level, the differences are about 0.5 dB for the second measurement.

VI. DISCUSSIONS AND CONCLUSION

Impacts of real hands of a cellphone operating person on radiation properties of antenna arrays at two millimeter-wave frequencies, 28 and 39 GHz, are explored in this article. The cellphone antenna arrays are designed so that they have 2-GHz impedance bandwidth to respond to a possible frequency shift due to manufacturing errors. Full-complexity cellphone models including feed lines and cable connectors along with their simplified models with no feed lines and only discrete ports serve different purposes in the antenna evaluation; the former is used for the antenna–hand interaction measurements, while the latter is a reference for de-embedding losses of the antenna measurement setup. Both in the free-space and hand-involved cases, the similarity between the simulated and measured spherical coverage characteristics was observed. The measurement setup required special attention when involving human hands because of their nonrepeatable nature. For example, far-field measurements were not feasible in our anechoic chamber and hence we resorted to the near-field characterization of the radiated fields. Furthermore, phone mock-ups were fixed at specific postures, i.e., either horizontally or vertically, so that the necessary electric near-field distribution was measured with a manageable time duration for a human operator to stay still. The validity of the elaborated near-field measurement setup of antenna arrays with real human hands was confirmed by the mentioned comparisons of the spherical coverage characteristics between the simulations and measurements. Their CCDF from repeated antenna–hand measurements revealed up to a 0.5-dB difference at the median level.

To conclude: 1) the manufactured referential antenna arrays, which serve as cellphone mock-ups for measurements with hand effects, show similar radiation characteristics as simplified cellphone arrays; 2) the simulation models generated by the approach proposed in [1] are proved to be accurate enough serving for hand effect simulations; 3) measurement setups are proved to be accurate and stable for radiation measurements involving real hand effects; and 4) the simulations involving hand effects on radiations of cellphone antennas are proved to represent the reality so that researchers can trust the simulations results involving hand effects and study hand effects by simulations instead of complex measurements in the future.

APPENDIX

Based on the Huygens principle, the equivalent sources on the scanning plane can be defined to replace the original source

of the antenna array. On a surface S_0 of an area $L_x L_y$ in front of the antennas, the equivalent magnetic current sources at a point (x_i', y_j', d) can be obtained by an observation of the electric field at the same location, E, as

$$M(n) = -\hat{n} \times E(n) \quad \text{on } S_0 \tag{2}$$

where bold symbols mean that they are vector or matrix; $\hat{n}$ is a unit normal vector of the scanning plane, which corresponds to $\hat{z}$ in Fig. 7(a); the symbol $\times$ denotes the outer product; $1 \leq i \leq N_x$ and $1 \leq j \leq N_y$ are the indices of the probe measurement points along the x- and y-axes, respectively, and finally, $n = i + (j-1)N_x$, $1 \leq n \leq N = N_x N_y$ denotes a unique index of probe measurement points. The far field E_{far} can be represented by

$$E_{\text{far}} = -\nabla \times \int_{S_0} M(r')g(r, r')\mathrm{d}s' \tag{3}$$

where $\nabla \times$ is the curl operator in the Cartesian coordinate system and includes the transformation from the Cartesian to spherical coordinate systems; $E_{\text{far}} = [E_\theta \ E_\phi \ E_r]^\top$ in the spherical coordinate system and $M = [M_x \ M_y \ 0]^\top$ in the Cartesian coordinate system, where $E_r \approx 0$ when $r \to \infty$ and $\cdot^\top$ represents a transpose operation; $g(r, r') = (e^{-jk_0 r}/4\pi r)e^{jk_0((r \cdot r')/r)}$ is Green's function in free space at infinite distance; $r \cdot r' = x_{\text{far}}x' + y_{\text{far}}y' + z_{\text{far}}z'$; $r' = ((x')^2 + (y')^2 + d^2)^{1/2}$ is a distance from the origin of the coordinate system to the probe measurement point (x', y', d); $r = ((x_{\text{far}})^2 + (y_{\text{far}})^2 + (z_{\text{far}})^2)^{1/2}$ is a distance from the origin of the coordinate system to the far-field point $(x_{\text{far}}, y_{\text{far}}, z_{\text{far}})$ as defined in Fig. 7(a); k_0 is the wave number in free space at the testing frequency, and finally, $j = \sqrt{-1}$. Though the origin can be set arbitrary, in this article, it is located at the middle of the antenna array. Then, the x- and y-components of the equivalent magnetic current source M in (2) can be collected across N near-field measurement points to form column vectors as

$$M_x = \begin{bmatrix} E_y(1) & E_y(2) & \cdots & E_y(N) \end{bmatrix}^\top \tag{4}$$

$$M_y = -\begin{bmatrix} E_x(1) & E_x(2) & \cdots & E_x(N) \end{bmatrix}^\top. \tag{5}$$

Then, θ- and ϕ-components of the far-field E_{far} observed at $(x_{\text{far},k}, y_{\text{far},k}, z_{\text{far},k})$, $1 \leq k \leq K$, can be obtained by

$$\begin{bmatrix} E_{\theta,k} \\ E_{\phi,k} \end{bmatrix} = \begin{bmatrix} H_{k,11} & H_{k,12} \\ H_{k,21} & H_{k,22} \end{bmatrix} \begin{bmatrix} M_x \\ M_y \end{bmatrix} \tag{6}$$

where $H_{k,11}$, $H_{k,12}$, $H_{k,21}$, $H_{k,22} \in \mathbb{C}^N$ are the row vectors. Their nth entries, denoted as $[\cdot]_n$, can be represented, respectively, by

$$[H_{k,11}]_n = \left\{ \begin{array}{l} \cos\theta_k \sin\phi_k(z_{\text{far},k}) \\ + \sin\theta_k(y_{\text{far},k}) \end{array} \right\} G'(r_k, r_n')\Delta x \Delta y \tag{7}$$

$$[H_{k,12}]_n = -\left\{ \begin{array}{l} \cos\theta_k \cos\phi_k(z_{\text{far},k}) \\ + \sin\theta_k(x_{\text{far},k}) \end{array} \right\} G'(r_k, r_n')\Delta x \Delta y \tag{8}$$

$$[H_{k,21}]_n = \left\{ \cos\phi_k(z_{\text{far},k}) \right\} G'(r_k, r_n')\Delta x \Delta y \tag{9}$$

$$[H_{k,22}]_n = \left\{ \sin\phi_k(z_{\text{far},k}) \right\} G'(r_k, r_n')\Delta x \Delta y \tag{10}$$

where $G'(r_k, r_n') = (e^{-jk_0 r_k}/4\pi r_k^2)(jk_0 + (1/r_k))e^{jk_0((r_k \cdot r_n')/r_k)}$ and r_k is the distance between the kth far-field point and the coordinate origin; r_n' is the distance between the nth probe

measurement point and the coordinate origin. Using the formulas, the radiation patterns of the antenna under the test can be obtained based on the planar near-field measurements.

REFERENCES

[1] L. Vaha-Savo, P. Koivumaki, K. Haneda, C. Icheln, and J. Chen, "3-D modeling of human hands for characterizing antenna radiation from a 5G mobile phone," in *Proc. 16th Eur. Conf. Antennas Propag. (EuCAP)*, Mar. 2022, pp. 1–5.

[2] *Study on Test Methods (Release 16)*. document TR 38.810, version 16.1.0, 3GPP, Dec. 2018. [Online]. Available: http://www.3gpp.org/dynareport/38810.htm

[3] J. Helander, K. Zhao, Z. Ying, and D. Sjöberg, "Performance analysis of millimeter-wave phased array antennas in cellular handsets," *IEEE Antennas Wireless Propag. Lett.*, vol. 15, pp. 504–507, 2016.

[4] W. Hong, K.-H. Baek, and S. Ko, "Millimeter-wave 5G antennas for smartphones: Overview and experimental demonstration," *IEEE Trans. Antennas Propag.*, vol. 65, no. 12, pp. 6250–6261, Dec. 2017.

[5] B. Xu et al., "Radiation performance analysis of 28 GHz antennas integrated in 5G mobile terminal housing," *IEEE Access*, vol. 6, pp. 48088–48101, 2018.

[6] J. Krogerus, J. Toivanen, C. Icheln, and P. Vainikainen, "Effect of the human body on total radiated power and the 3-D radiation pattern of mobile handsets," *IEEE Trans. Instrum. Meas.*, vol. 56, no. 6, pp. 2375–2385, Dec. 2007.

[7] I. Syrytsin, S. Zhang, G. F. Pedersen, K. Zhao, T. Bolin, and Z. Ying, "Statistical investigation of the user effects on mobile terminal antennas for 5G applications," *IEEE Trans. Antennas Propag.*, vol. 65, no. 12, pp. 6596–6605, Dec. 2017.

[8] I. Syrytsin, S. Zhang, and G. F. Pedersen, "User impact on phased and switch diversity arrays in 5G mobile terminals," *IEEE Access*, vol. 6, pp. 1616–1623, 2018.

[9] U. T. Virk and K. Haneda, "Modeling human blockage at 5G millimeter-wave frequencies," *IEEE Trans. Antennas Propag.*, vol. 68, no. 3, pp. 2256–2266, Mar. 2020.

[10] K. Haneda, M. Heino, and J. Jaervelaeinen, "Total array gains of millimeter-wave mobile phone antennas under practical conditions," in *Proc. IEEE 87th Veh. Technol. Conf. (VTC Spring)*, Jun. 2018, pp. 1–6.

[11] K. Haneda, M. Heino, and J. Järveläinen, "Total array gains of polarized millimeter-wave mobile phone antennas," in *Proc. Eur. Conf. Netw. Commun. (EuCNC)*, Jun. 2018, pp. 167–171.

[12] K. Zhao, J. Helander, D. Sjöberg, S. He, T. Bolin, and Z. Ying, "User body effect on phased array in user equipment for the 5G mmWave communication system," *IEEE Antennas Wireless Propag. Lett.*, vol. 16, pp. 864–867, 2017.

[13] J. Hejselbæk, J. Ø. Nielsen, W. Fan, and G. F. Pedersen, "Measured 21.5 GHz indoor channels with user-held handset antenna array," *IEEE Trans. Antennas Propag.*, vol. 65, no. 12, pp. 6574–6583, Dec. 2017.

[14] K. Zhao, Z. Ying, S. Zhang, and G. Pedersen, "User body effects on mobile antennas and wireless systems of 5G communication," in *Proc. 14th Eur. Conf. Antennas Propag. (EuCAP)*, Mar. 2020, pp. 1–5.

[15] M. Heino, C. Icheln, and K. Haneda, "Self-user shadowing effects of millimeter-wave mobile phone antennas in a browsing mode," in *Proc. 13th Eur. Conf. Ant. Prop. (EuCAP)*, Krakow, Poland, Apr. 2019, pp. 1–5.

[16] L. Vaha-Savo et al., "Empirical evaluation of a 28 GHz antenna array on a 5G mobile phone using a body phantom," *IEEE Trans. Antennas Propag.*, vol. 69, no. 11, pp. 7476–7485, Nov. 2021.

[17] C. Ballesteros, L. Vähä-Savo, K. Haneda, C. Icheln, J. Romeu, and L. Jofre, "Assessment of mmWave handset arrays in the presence of the user body," *IEEE Antennas Wireless Propag. Lett.*, vol. 20, no. 9, pp. 1736–1740, Sep. 2021.

[18] F. Fernandes, C. Rom, J. Harrebek, S. Svendsen, and C. N. Manchón, "Hand blockage impact on 5G mmWave beam management performance," *IEEE Access*, vol. 10, pp. 106033–106049, 2022.

[19] P. Liu, I. Syrytsin, J. Ø. Nielsen, G. F. Pedersen, and S. Zhang, "Characterization and modeling of the user blockage for 5G handset antennas," *IEEE Trans. Instrum. Meas.*, vol. 70, pp. 1–11, 2021.

[20] P. Liu, I. Syrytsin, and S. Zhang, "Investigation on user shadow suppression for mobile handset antenna at 28 GHz," in *Proc. 16th Eur. Conf. Antennas Propag. (EuCAP)*, Mar. 2022, pp. 1–5.

[21] M. Heino, C. Icheln, and K. Haneda, "Finger effect on 60 GHz user device antennas," in *Proc. 10th Eur. Conf. Antennas Propag. (EuCAP)*, Apr. 2016, pp. 1–5.

[22] V. Raghavan et al., "Spatio-temporal impact of hand and body blockage for millimeter-wave user equipment design at 28 GHz," *IEEE Commun. Mag.*, vol. 56, no. 12, pp. 46–52, Dec. 2018.

[23] V. Raghavan, M.-L. C. Chi, M. A. Tassoudji, O. H. Koymen, and J. Li, "Antenna placement and performance tradeoffs with hand blockage in millimeter wave systems," *IEEE Trans. Commun.*, vol. 67, no. 4, pp. 3082–3096, Jan. 2019.

[24] S. S. Zhekov and G. F. Pedersen, "Effect of dielectric properties of human hand tissue on mobile terminal antenna performance," in *Proc. 14th Eur. Conf. Antennas Propag. (EuCAP)*, Mar. 2020, pp. 1–5.

[25] T. Q. K. Nguyen, M. S. Miah, L. Lizzi, K. Haneda, and F. Ferrero, "Experimental evaluation of user's finger effects on a 5G terminal antenna array at 26 GHz," *IEEE Antennas Wireless Propag. Lett.*, vol. 19, no. 6, pp. 892–896, Jun. 2020.

[26] V. Raghavan et al., "Hand and body blockage measurements with form-factor user equipment at 28 GHz," *IEEE Trans. Antennas Propag.*, vol. 70, no. 1, pp. 607–620, Jul. 2022.

[27] F. Yu, L. Zeng, D. Pan, X. Sui, and J. Tang, "Evaluating the accuracy of hand models obtained from two 3D scanning techniques," *Sci. Rep.*, vol. 10, no. 1, pp. 1–10, Jul. 2020.

[28] R. Khan, A. A. Al-Hadi, and P. J. Soh, "Recent advancements in user effect mitigation for mobile terminal antennas: A review," *IEEE Trans. Electromagn. Compat.*, vol. 61, no. 1, pp. 279–287, Feb. 2019.

[29] C. Buey, F. Ferrero, L. Lizzi, P. Ratajczak, Y. Benoit, and L. Brochier, "Investigation of hand effect on a handheld terminal at 11 GHz," in *Proc. 10th Eur. Conf. Antennas Propag. (EuCAP)*, Apr. 2016, pp. 1–5.

[30] Y. Zhu, Z. Zhao, and C. Deng, "Millimeter-wave dual-polarized frame-integrated patch antenna array for 5G mobile handsets," in *Proc. IEEE 3rd Int. Conf. Electron. Inf. Commun. Technol. (ICEICT)*, Nov. 2020, pp. 613–615.

[31] L. Wen et al., "Millimeter-wave dual-polarized active phased array antenna for 5G applications," in *Proc. 24th Int. Microw. Radar Conf. (MIKON)*, Sep. 2022, pp. 1–3.

[32] Rogers. *Copper Foils for High Frequency Materials*. Accessed: 2021. [Online]. Available: https://www.rogerscorp.cn/-/media/project/rogerscorp/doc-uments/advanced-electronics-solutions/english/properties—detailed-characteristics/copper-foils-for-high-frequency-circuit-materials.pdf

[33] S. Gabriel, R. W. Lau, and C. Gabriel, "The dielectric properties of biological tissues: III. Parametric models for the dielectric spectrum of tissues," *Phys. Med. Biol.*, vol. 41, no. 11, p. 2271, 1996.

[34] E. Joy, W. Leach, and G. Rodrigue, "Applications of probe-compensated near-field measurements," *IEEE Trans. Antennas Propag.*, vol. AP-26, no. 3, pp. 379–389, May 1978.

[35] A. D. Yaghjian, "Approximate formulas for the far field and gain of open-ended rectangular waveguide," *IEEE Trans. Antennas Propag.*, vol. AP-32, no. 4, pp. 378–384, Apr. 1984.

[36] A. Hazmi et al., "Spherical coverage characterization of millimeter wave antenna arrays in 5G mobile terminals," in *Proc. 13th Eur. Conf. Ant. Prop. (EuCAP)*, Krakow, Poland, Apr. 2019, pp. 1–5.

[37] A. Hazmi and R. Tian, "Throughput and spherical coverage performance of mmWave dual polarized antenna arrays," in *Proc. 14th Eur. Conf. Antennas Propag. (EuCAP)*, Mar. 2020, pp. 1–4.

[38] *Discussion of mmWave UE Eirp and EIS Test*. document R4-1700095, 3rd Generation Partnership Project (3GPP), Jan. 2017.

Bing Xue (Graduate Student Member, IEEE) was born in Henan, China. He is currently pursuing the D.Sc. (Tech.) degree in radio engineering in the School of Electrical Engineering, Aalto University, Espoo, Finland.

His current research interests include antenna designs and measurements, human–antenna interaction simulation and measurements, and electromagnetic modeling focusing on mm-Wave frequencies for 5G systems and beyond.

Pasi Koivumäki (Member, IEEE) received the M.Sc. (Tech.) (Hons.) degree from the School of Electrical Engineering, Aalto University, Espoo, Finland, in 2017, where he is currently pursuing the D.Sc. (Tech.) degree in radio engineering.

His current research activities include multiband radio channel measurements, simulations, and modeling focusing on mm-wave frequencies for 5G systems and beyond. His particular interests lie in ray-launching and ray-tracing algorithms for propagation and channel modeling in urban environments of future smart cities and their combined effects on cellular coverage and quality of service.

Katsuyuki Haneda (Member, IEEE) is currently an Associate Professor with the School of Electrical Engineering, Aalto University, Espoo, Finland. He was an author and co-author of several best paper and student paper awards in the IEEE Vehicular Technology Conference and European Conference on Antennas and Propagation, among others. His current research activity covers high-frequency radios such as millimeter-wave and beyond and wireless for medical and smart-city applications.

Prof. Haneda received the R. W. P. King Paper Award of the IEEE TRANSACTIONS ON ANTENNAS AND PROPAGATION in 2021, together with Dr. Usman Virk. He was an Associate Editor of the IEEE TRANSACTIONS ON ANTENNAS AND PROPAGATION in 2012 and 2016, and also an Editor of the IEEE TRANSACTIONS ON WIRELESS COMMUNICATIONS in 2013 and 2018. He was a Guest Editor of Special Issues on Antennas and Propagation Aspects of In-Band Full-Duplex Applications and on Artificial Intelligence in Radio Propagation for Communications in the IEEE TRANSACTIONS ON ANTENNAS AND PROPAGATION in 2021 and 2022, respectively. He is also a Guest Editor of the forthcoming Special Section on Sub-THz and THz Radio Propagation: Measurements and Characterization in the IEEE Open Journal of Antennas and Propagation. He was a Co-Chair of a disciplinary working group on radio channels in European COST Actions CA15104 Inclusive Radio Communication Networks for 5G and beyond (IRACON) from 2016 to 2020. He is a Technical Programme Committee Co-Chair of the 17th European Conference on Antennas and Propagation (EuCAP 2023), Florence, Italy.

Lauri Vähä-Savo (Graduate Student Member, IEEE) received the B.E. and M.E. degrees from the School of Electrical Engineering, Aalto University, Espoo, Finland, in 2016 and 2019, respectively, where he is currently pursuing the Ph.D. degree with the Department of Electronics and Nanosciences, Antennas and Propagation Group.

He is currently working in the field of 5G antennas and outdoor-to-indoor communication. His research interests include microwave and millimeter-wave antenna design, human–antenna interaction, smart building, and cities.

Clemens Icheln received the Dipl.-Ing. degree in electrical engineering from the Hamburg-Harburg University of Technology, Hamburg, Germany, in 1996, and the Licentiate degree and the D.Sc.Tech. degree in radio engineering from Aalto University, Espoo, Finland, in 1999 and 2001, respectively.

He is currently a University Lecturer with the Department of Electronics and Nanoengineering, School of Electrical Engineering, Aalto University, Espoo, Finland. His current research interests include design of multielement antennas for small communication devices such as mobile terminals and medical implants, to operate at frequency ranges as low as 400 MHz but also up to mm-wave frequencies, as well as the development of suitable antenna characterization methods that allow taking, e.g., the effects of the radio channel into account.